

# Calibration of Surface Brightness Fluctuations for Dwarf Galaxies in the Hyper Suprime-Cam $gi$ Filter System

YOO JUNG KIM<sup>1</sup> AND MYUNG GYOON LEE<sup>1</sup>

<sup>1</sup>*Astronomy Program, Department of Physics and Astronomy, SNUARC, Seoul National University, 1 Gwanak-ro, Gwanak-gu, Seoul 08826, Republic of Korea*

(Accepted October 5, 2020)

Submitted to ApJ

## ABSTRACT

Surface brightness fluctuation (SBF) magnitudes are a powerful standard candle to measure distances to semi-resolved galaxies in the local universe, a majority of which are dwarf galaxies that have often bluer colors than bright early-type galaxies. We present an empirical  $i$ -band SBF calibration in a blue regime,  $0.2 \lesssim (g-i)_0 \lesssim 0.8$  in the Hyper Suprime-Cam (HSC) magnitude system. We measure SBF magnitudes for 12 nearby dwarf galaxies of various morphological types with archival HSC imaging data, and use their tip of the red giant branch (TRGB) distances to derive fluctuation - color relations. In order to subtract contributions of fluctuations due to young stellar populations, we use five different  $g$ -band magnitude masking thresholds,  $M_{g,\text{thres}} = -3.5, -4.0, -4.5, -5.0$ , and  $-5.5$  mag. We find that the rms scatter of the linear fit to the relation is the smallest (rms = 0.16 mag) in the case of  $M_{g,\text{thres}} = -4.0$  mag,  $\overline{M}_i = (-2.65 \pm 0.13) + (1.28 \pm 0.24) \times (g-i)_0$ . This scatter is much smaller than those in the previous studies (rms=0.26 mag), and is closer to the value for bright red galaxies (rms=0.12 mag). This calibration is consistent with predictions from metal-poor simple stellar population models.

**Keywords:** Standard candles (1563); Distance indicators (394); Dwarf galaxies (416); Galaxy distances (590); Stellar populations (1622)

## 1. INTRODUCTION

With recent deep and wide ground-based imaging surveys, a large number of dwarf galaxies in the Local Volume (LV) have been newly discovered (e.g. Carlin et al. 2016; Cohen et al. 2018; Carlsten et al. 2020a; Davis et al. 2021). These dwarf galaxies have been used for various purposes, such as testing structure formation theories in small scales (e.g. "Missing Satellites" problem; Klypin et al. (1999); Moore et al. (1999); Bullock & Boylan-Kolchin (2017); Müller & Jerjen (2020); Carlsten et al. (2021)) and studying the environmental effects on dwarf galaxies (Carlin et al. 2021; Davis et al. 2021). For these purposes, it is crucial to obtain precise distances to dwarf galaxies.

If the old stellar populations of a galaxy are resolved, one can obtain its distance from photometry of red giant

branch stars (the tip of the red giant branch (TRGB) method; Lee et al. 1993). However, for farther galaxies, of which stellar populations are semi-resolved, the surface brightness fluctuation (SBF) method can be useful (Tonry & Schneider 1988).

Basically, the SBF technique measures spatial fluctuations in a galaxy image, resulting from Poisson statistics in the number of stars per resolution element (Tonry & Schneider 1988). The fluctuation amplitudes due to old red giant branch (RGB) stars and asymptotic red giant branch (AGB) stars in a galaxy may be used as a standard candle. The technique has been mostly applied to massive early-type galaxies which consist mainly of old stellar populations.

The fluctuation amplitudes are measured in Fourier space and contributions from non-stellar contaminating sources such as background objects and globular clusters are subtracted. The fluctuation amplitudes are then converted to distances using empirical *SBF calibrations*, which are relations between the fluctuation magnitude

and integrated galaxy color (Tonry et al. 1990; Jensen et al. 2003; Blakeslee et al. 2009; Jensen et al. 2015).

The color dependence of the fluctuation reflects that the fluctuation magnitudes depend on stellar populations, as studied by stellar population models (e.g. Liu et al. 2000; Blakeslee et al. 2001; Jensen et al. 2003). In the regime of massive galaxies with old stellar populations, redder galaxies which consist of more metal-rich stellar populations show fainter SBF magnitudes than bluer galaxies with lower metallicity. The relation between the integrated color and the fluctuation magnitude is widely studied using the Hubble Space Telescope (HST) (Blakeslee et al. 2009, 2010; Jensen et al. 2015) and ground-based telescopes (Cantiello et al. 2018; Carlsten et al. 2019b). The relation is known to be tight in the red color regime. For example, even with the ground-based Canada-France-Hawaii Telescope (CFHT), the rms scatter in the  $i$ -band is as small as 0.12 mag (Cantiello et al. 2018). The rms scatter is even smaller than 0.1 mag in the F814W band based on the HST data (Blakeslee et al. 2010).

However, the relation in the bluer regime for dwarf galaxies is not a simple extrapolation of the redder counterpart. Several groups have explored the use of the SBF method to determine distances to dwarf elliptical galaxies, which are metal-poor and thus bluer, in the LV. They found that the color dependence is less than those for bright red galaxies (Jerjen et al. 1998, 2000, 2001; Cantiello et al. 2018) and the intrinsic scatter is larger (Mieske et al. 2006; Blakeslee et al. 2009; Jensen et al. 2015), complicating an accurate distance measurement for dwarf galaxies. The scatter is attributed by a larger sampling scatter (Blakeslee et al. 2009), presence of younger stellar populations (Jerjen et al. 1998), or both (Greco et al. 2021).

In particular, larger uncertainties are introduced in measuring SBF of galaxies with young stellar populations (Jensen et al. 2015; Carlsten et al. 2019b). Young stars in star forming regions are often clumped and very luminous, introducing a significant fluctuation. In addition, dust and nebular emission affect SBF signals. Therefore, one should avoid using regions with young stellar populations in measuring the SBF.

Recently, Carlsten et al. (2019b) derived a new relation between  $i$ -band SBF magnitude and integrated  $g-i$  color in the blue regime ( $0.3 \lesssim (g-i)_0 \lesssim 0.8$ ) using 32 LV dwarf galaxies with TRGB distances measured with CFHT (28 galaxies) and HST (6 galaxies in Cohen et al. (2018)). With the inclusion of star-forming galaxies to the calibration sample, they extended the use of SBF to the regime of dwarf galaxies with young stars. In measuring the SBF, they masked point sources brighter

than a threshold chosen in the range  $-6 < M_g, M_i < -4$  mag and removed contributions of fainter objects by subtracting fluctuation powers measured in nearby background fields. Using this relation between SBF magnitude and integrated color, they confirmed group memberships of multiple blue dwarf galaxies in the LV (Carlsten et al. 2019a, 2021). However, the rms scatter of their calibration is as large as 0.26 mag, leading to a 15% uncertainty in distance measurements.

In this study, we present a new SBF calibration in the blue regime ( $0.2 \lesssim (g-i)_0 \lesssim 0.8$ ) using dwarf galaxies with TRGB distances in archival Subaru/Hyper Suprime-Cam (HSC) imaging data. In particular, using a fixed masking threshold magnitude for contaminating sources, we reduced the rms scatter down to 0.16 mag. The paper is structured as follows. In Section 2, we describe the HSC data and our selection of galaxies used for calibration. In Section 3, we illustrate the methods of SBF distance measurements, with details on masking contaminating sources. In Section 4, we derive an  $i$ -band SBF calibration. In Section 5, we compare our calibration with recent ground-based empirical calibrations and with stellar population models. In Section 6, we summarize our primary results.

## 2. DATA AND GALAXY SAMPLE

For the SBF calibration, we search for dwarf galaxies that have HSC images with sufficient  $g$ - and  $i$ -band exposures in the SMOKA Science Archive<sup>1</sup>. Among them we selected nearby galaxies with TRGB distances smaller than 10 Mpc found in the Updated Nearby Galaxy Catalog (Karachentsev et al. 2013). Galaxies with extremely low surface brightness (central surface brightness fainter than  $24.5 \text{ mag arcsec}^{-2}$ ) were excluded from the sample. Moreover, galaxies of which the area bright enough to measure SBF is smaller than  $50 \text{ arcsec}^2$  were excluded as well. In total, we selected 12 dwarf galaxies.

Figure 1 shows pseudo color images based on HSC  $g$  and  $i$ -band images (top panels) and gray scale  $i$ -band images (bottom panels) of the selected galaxies in our sample. In Table 1 we list basic information of the galaxies sorted by the TRGB distances. F814W TRGB magnitudes of all the galaxies were obtained from Extragalactic Distance Database (EDD)(Tully et al. 2009; Jacobs et al. 2009; Anand et al. 2021)<sup>2</sup>. Since the dwarf galaxies have blue TRGB colors, we use the most recent color-independent TRGB calibration in Jang et al. (2021) ( $M_{\text{F814W}}^{\text{TRGB}} = -4.050 \pm 0.028 \text{ (stat)} \pm 0.048 \text{ (sys)}$ )

<sup>1</sup> <https://smoka.nao.ac.jp/>

<sup>2</sup> <http://edd.ifa.hawaii.edu/>

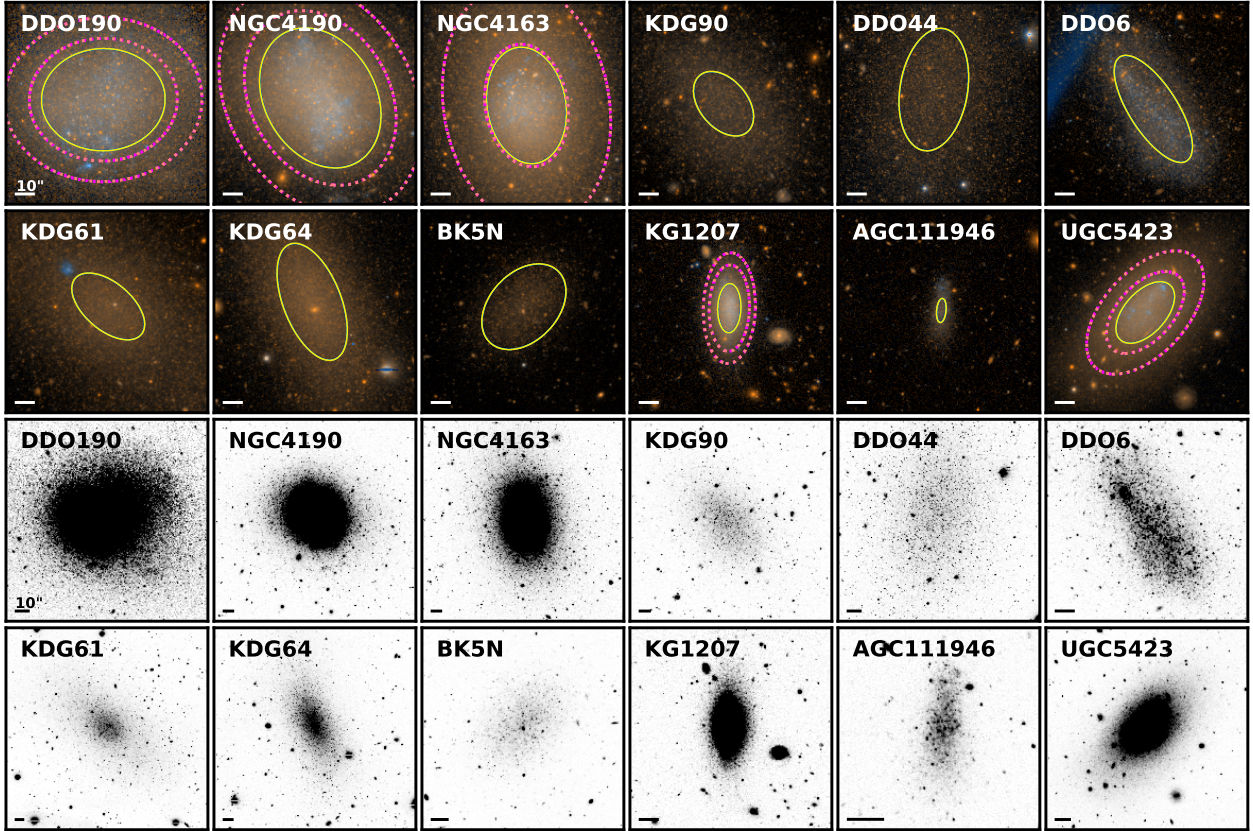


**Figure 1.** HSC images of our selected dwarf galaxies for the SBF calibration. (Top)  $2' \times 2'$  pseudo-color images based on  $g$ - and  $i$ -band images. Solid lines indicate the boundary of the inner field in a galaxy and dotted lines indicate that of the outer field. (Bottom) Gray scale  $i$ -band images of the same galaxies but with different fields of view to show better faint stellar light. North is up and east to the left. The scale bars in each image represent 10 arcsec.

to convert TRGB magnitudes to distances. Note that the TRGB calibration we use in this study is consistent with the calibration in [Blakeslee et al. \(2021\)](#) in tying the SBF method to the TRGB for massive early-type galaxies. The TRGB distances to these galaxies are from 2.76 to 8.71 Mpc. Total magnitudes of the galaxies range from  $M_B \approx -10.6$  to  $-15.6$  mag. Our sample is composed of various morphological types: 3 spheroidal galaxies, 7 late-type galaxies (BCD, Ir, and Im), and 2 transition types between early-type and late-type galaxies.

Among our sample, five galaxies (DDO 190, NGC 4190, NGC 4163, KG 1207, and UGC 5423) show a notable presence of young blue stars and higher surface brightness in the central regions compared with the outer regions. Thus, the stellar populations in the inner and the outer parts of these galaxies are likely to differ. We divide each of these galaxies into an inner field and an outer halo field. The areas of the chosen fields are indicated as solid lines and dotted lines in the top panels of Figure 1. Therefore, the sample for SBF measurements consists of 17 fields in 12 galaxies.

The HSC images are fully reduced, sky subtracted, and coadded with the pipeline `hscPipe` designed for LSST ([Bosch et al. \(2018\)](#); [Ivezić et al. \(2019\)](#)). Global sky subtraction was carried out in two steps in `hscpipe v6` ([Aihara et al. 2019](#)). Empirical background model was made by averaging pixels (ignoring detected objects) in  $1024 \times 1024$  superpixel grids in the entire focal plane, then fitting the values with a 6th order two-dimensional Chebyshev polynomial. Smaller scale features were subtracted by fitting a scaled sky frame, which is the mean response of the instrument to the sky for a particular filter. This sky subtraction technique preserves low surface brightness features better than previous versions of `hscpipe`. The pixel scale of HSC images is  $0.168''$  per pixel, and  $i$ -band seeing for these images are  $0.5''$ - $0.7''$ .

For the following analysis, we correct for foreground reddening on each galaxy based on the extinction maps by [Schlegel et al. \(1998\)](#) and the conversion coefficients obtained by [Schlafly & Finkbeiner \(2011\)](#), as listed in Table 1. All the magnitudes are in the AB system and



**Table 1.** List of Dwarf Galaxies Used for SBF Calibration

Name	R.A. (J2000)	Decl. (J2000)	$D_{TRGB}^a$ (Mpc)	$M_B^b$ (mag)	$A_i^c$ (mag)	Morphology <sup>d</sup> (mag)	$t_{exp} (g/i)^e$ (s)
DDO 190	14 : 24 : 43.5	44 : 31 : 33	$2.76 \pm 0.08$	-14.1	0.02	Im	810/1230
NGC 4190	12 : 13 : 44.6	36 : 38 : 00	$2.84 \pm 0.11$	-13.9	0.05	BCD	7500/2580
NGC 4163	12 : 12 : 08.9	36 : 10 : 10	$2.95 \pm 0.08$	-13.8	0.03	Im	14070/5430
KDG 90	12 : 14 : 57.9	36 : 13 : 08	$3.02 \pm 0.12$	-11.5	0.03	Tr	7500/2580
DDO 44	07 : 34 : 11.3	66 : 53 : 10	$3.25 \pm 0.10$	-12.1	0.07	Sph	3150/1350
DDO 6	00 : 49 : 49.3	-21 : 00 : 58	$3.40 \pm 0.15$	-12.4	0.03	Ir	10935/2595
KDG 61	09 : 57 : 02.7	68 : 35 : 30	$3.63 \pm 0.10$	-12.9	0.12	Sph	13336/13654
KDG 64	10 : 07 : 01.9	67 : 49 : 39	$3.71 \pm 0.10$	-12.6	0.09	Tr	4430/6330
BK5N	10 : 04 : 40.3	68 : 15 : 20	$3.72 \pm 0.17$	-10.6	0.11	Sph	5530/7590
KG 1207	12 : 09 : 56.4	36 : 26 : 07	$4.88 \pm 0.32$	-13.0	0.04	Im	5550/1710
AGC 111946	01 : 46 : 41.6	26 : 48 : 05	$8.36 \pm 0.29$	-11.4	0.14	Ir	3150/2150
UGC 5423	10 : 05 : 30.6	70 : 21 : 52	$8.71 \pm 0.24$	-15.6	0.14	Ir	4430/6330

NOTE— <sup>a</sup> TRGB distances calculated from F814W TRGB magnitudes in EDD (Jacobs et al. 2009; Anand et al. 2021) with the recent blue-color TRGB calibration in Jang et al. (2021).

<sup>b</sup> *B*-band absolute total magnitudes from the Updated Nearby Galaxy Catalog (Karachentsev et al. 2013).

<sup>c</sup> Foreground reddening based on the extinction maps by Schlegel et al. (1998) and the conversion coefficients obtained by Schlafly & Finkbeiner (2011).

<sup>d</sup> Dwarf galaxy morphological types classified by Karachentsev et al. (2013) (Sph for spheroidal galaxies, Im for Magellanic type irregular galaxies, Ir for irregular galaxies, BCD for blue compact dwarfs, and Tr for transition types between spheroidals and irregulars.)

<sup>e</sup> Exposure times for HSC *g* and *i*-band images.

extinction- corrected magnitudes and colors are denoted with subscript 0 throughout the paper.

### 3. SBF MEASUREMENT

In this section, we describe our method of applying SBF techniques to the sample galaxies. We present the SBF measurements for two example galaxies as shown in Figure 2: one spheroidal galaxy (BK5N) and one irregular galaxy (DDO 6), both located at similar distances (3.40 Mpc and 3.72 Mpc, respectively.) DDO 6 is the bluest and BK5N is the reddest in the sample.

#### 3.1. SBF Method

The SBF distance indicator was first introduced by Tonry & Schneider (1988) and has been widely used to measure distances to semi-resolved galaxies. The overall procedure of SBF measurements is well described in Tonry & Schneider (1988). The fluctuation image is calculated as  $(\text{Galaxy} - \text{Model})/\sqrt{\text{Model}}$  (see Fig 2(c) and (i) for BK5N and DDO 6, respectively), where Galaxy denotes the observed galaxy image (Fig 2(a) and (g)) and Model corresponds to the smooth galaxy light component (Fig 2(b) and (h)). Since our sample is composed of not only early-type galaxies but also late-type galaxies, we use median-filtered galaxy images as described

below in Section 3.2 to obtain smooth galaxy light components instead of function-fitting galaxy models which have been often adopted for early-type galaxies (see Section 3.2).

The one-dimensional azimuthally averaged power spectrum is obtained from the fluctuation image in the Fourier domain (see Fig 2(e) and (k)). The power spectrum  $P(k)$  can be decomposed into the sum of a white noise component and the power spectrum of the point-spread function (PSF), scaled to match the stellar fluctuation amplitude. Therefore, it is fit by a linear function,

$$P(k) = P_0 E(k) + P_1. \quad (1)$$

$E(k)$  is the expectation power spectrum, which is the convolution of the normalized PSF power spectrum and the power spectrum of the mask. The mask is explained in Section 3.3 in detail.  $P_1$  represents the white-noise component and  $P_0$  represents the SBF amplitude, our quantity of interest. Right panels in Figure 2 show that the  $P_1$  is not constant but slightly sloped at the large wavenumbers. This is because pixel interpolations took place in stacking images by `hscpipe`. For this reason, fitting the largest wavenumbers should be avoided, as will be discussed in Section 3.4.

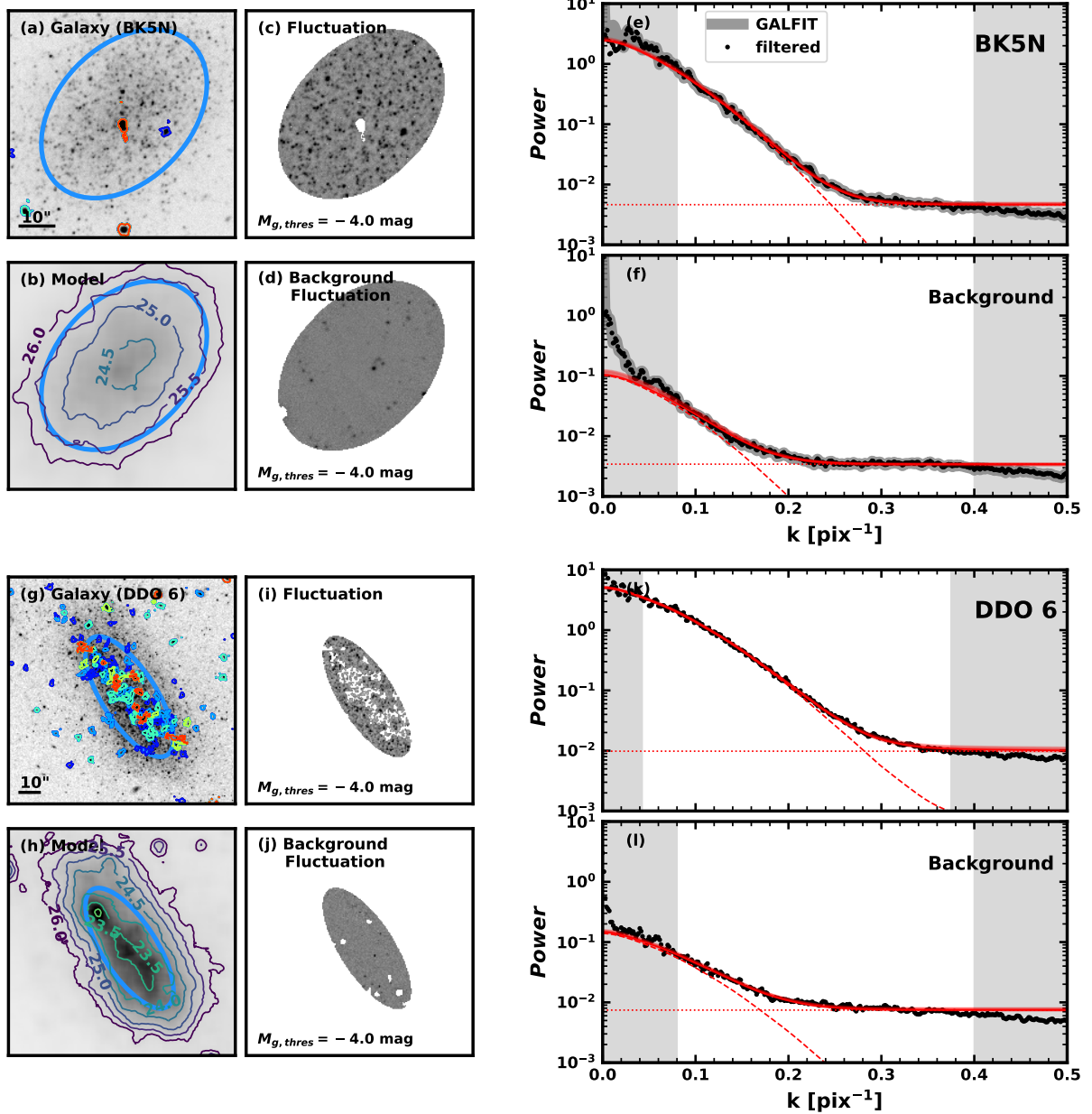


**Figure 2.** A summary of the components that go into the SBF measurement procedures for an early-type galaxy BK5N and an asymmetric late-type galaxy DDO 6. The upper and lower panels show the SBF measurement of BK5N and DDO 6, respectively. Panels (a) and (g) display *i*-band HSC images with blue ellipses representing the area used for SBF calculation. The small contours (dark blue, light blue, cyan, light green, and orange) indicate sources masked using thresholds of  $M_{g, \text{thres}} = -3.5, -4.0, -4.5, -5.0,$  and  $-5.5$  mag. Black bars represent  $10''$  length. Panels (b) and (h) show median-filtered model images used as smooth galaxy models. Contours show the surface brightness as an unit of  $\text{mag arcsec}^{-2}$ . Panels (c) and (i) are fluctuation images, which are calculated as  $(\text{Galaxy} - \text{Model})/\sqrt{\text{Model}}$ . Panels (d) and (j) are examples of background fluctuations sampled from a random area with no apparent bright objects and calculated as  $(\text{Background})/\sqrt{\text{Model}}$ . Panels (e) and (k) show azimuthally averaged power spectra of galaxy fluctuation images (black circles for median-filtered model images, and gray thick lines for GALFIT galaxy model images) and fitted lines (red solid lines). The units of power are arbitrary. Dashed lines and dotted lines indicate PSF-scale components and white noise components, respectively. Panels (f) and (l) show similar power spectra but for flat background fields within a radius of 0.2 degrees from the target galaxy. Gray regions at both ends are not used for fitting.

The apparent SBF magnitude is calculated by  $\bar{m} = -2.5 \log P_0 + zp$  where  $zp$  is the photometric zeropoint. The absolute SBF magnitude,  $\bar{M}_i$ , is obtained from fluctuation - integrated color relations, or SBF calibrations, derived empirically or theoretically (Tonry et al. 1990; Blakeslee et al. 2010; Jensen et al. 2015; Cantiello et al. 2018). Thus, once SBF  $P_0$  signals are measured and the integrated galaxy color is known, one can obtain galaxy distances from apparent SBF magnitudes.

In measuring the fluctuation power,  $P_0$ , one needs to mask or subtract sources that can contaminate the SBF, namely globular clusters, foreground stars, and background galaxies. The standard method which is applied mostly to early-type galaxies takes a statistical approach (Tonry & Schneider 1988; Jensen et al. 1998; Mei et al. 2005; Cantiello et al. 2005, 2018). First, find and apply masks to sources that are brighter than a certain magnitude threshold. Second, fit the luminosity functions of the sources with the combination of the globular cluster luminosity function (GCLF) and the background galaxy luminosity function. Third, extrapolate the luminosity functions to fainter magnitudes and calculate the contribution from unmasked sources. This power is then subtracted from the measured SBF power  $P_0$  to derive a corrected apparent SBF magnitude. This method is reasonable for massive galaxies with sufficiently large number of globular clusters that the luminosity function can be determined reliably.

### 3.2. Galaxy Modelling

As can be seen in Figure 1, many of our sample galaxies deviate from simple Sérsic models due to star-forming regions and asymmetric features. For example, while BK5N (Figure 2(a)) is well described by a single Sérsic model, DDO 6 (Figure 2(g)) has more complicated profiles. Therefore, instead of using simple galaxy models, we use median-filtered images as smooth galaxy models (Figure 2(b) and (h)). Then the fluctuation images are obtained by subtracting median-filtered galaxy images from the original galaxy images and normalizing them by the square root of the filtered images.

Using a median-filtered image as a substitute for galaxy model images is not conventional, but we could minimize the differences between the two methods by using an appropriate filter size. We tested this using galaxies that are well described by a single Sérsic model, such as BK5N (Figure 2a). In this case we derived a smooth galaxy model image using GALFIT (Peng et al. 2002) as well as a median-filtered galaxy image. Then we obtained azimuthally averaged power spectra of the fluctuation images, which are shown in Figure 2(e): black dots for the median-filtered galaxy image and gray thick lines for the GALFIT modelled galaxy image. Both agree

However, our sample galaxies are low-mass galaxies and many are late-types. The number of globular clusters in these galaxies is not large enough to derive a reasonable GCLF, requiring modification to the standard method. Recently, there have been efforts to obtain SBF distances to blue-regime dwarf galaxies which have young and blue stellar populations or low surface brightness (van Dokkum et al. 2018; Cohen et al. 2018; Carlsten et al. 2019b, 2021). Instead of modelling the contribution from globular clusters and background galaxies, Carlsten et al. (2019b) adopted a different way utilizing the background field fluctuation. They mask sources brighter than a magnitude threshold and estimate the contribution of the remaining faint sources by measuring the fluctuations in nearby background fields. Then they subtract it from the measured galaxy fluctuation. Examples of background fluctuation images for BK5N and DDO 6 are shown in Figure 2(d) and (j) and corresponding background power spectra in (f) and (l).

In this study, we follow the standard SBF measurement method (Tonry & Schneider 1988; Mei et al. 2005), but conduct masking and background subtraction similar to the method used by Carlsten et al. (2019b). For galaxy modelling, masking contaminating sources, and power spectra fitting, we provide a detailed description in the following subsections.

very well except for the largest scale ( $k < 0.03$ ). We tried multiple filter sizes to derive power spectra, and found the best match with those based on GALFIT models when the filter size =  $10 \times$  seeing size. Using too small a filter size removes some of PSF-scale fluctuations and using too large a filter size results in underestimating the galaxy light. Therefore, we use median filtered images as smooth galaxy models, assuming that they do not show any significant difference in their power spectra compared with standard methods. All the model images and power spectra in Figure 2 are derived with filter size being ten times the seeing size.

### 3.3. Masking Contaminating Sources

Essentially, masks are applied in order to exclude regions that contaminate true galaxy fluctuation signals or result in increasing measurement errors. There are two kinds of masks needed: (1) annular masks for area selection and (2) individual source masks for contaminating sources.

#### 3.3.1. Annular Mask for Area Selection

We choose an optimal area for SBF calculation of each field to minimize measurement errors. If one uses too

**Table 2.** SBF Results for the Dwarf Galaxies

Name		$D_{TRGB}$ (Mpc)	$(g-i)_0^\dagger$ (mag)	$\overline{\mu}_{i,0}^\dagger$ (mag arcsec $^{-2}$ )	SBF absolute magnitude $\overline{M}_i$ (mag)				
					Contaminating source masking threshold $M_{g,\text{thres}}$ (mag)				
					−3.5	−4.0	−4.5	−5.0	−5.5
DDO 190	inner	$2.76 \pm 0.08$	$0.29 \pm 0.03$	$22.25 \pm 0.02$	$-2.04 \pm 0.02$	$-2.20 \pm 0.02$	$-2.31 \pm 0.02$	$-2.44 \pm 0.03$	$-2.46 \pm 0.04$
	outer	$2.76 \pm 0.08$	$0.45 \pm 0.04$	$23.39 \pm 0.03$	$-1.94 \pm 0.02$	$-1.97 \pm 0.02$	$-1.93 \pm 0.06$	$-2.59 \pm 0.04$	$-2.62 \pm 0.04$
NGC 4190	inner	$2.84 \pm 0.11$	$0.33 \pm 0.02$	$21.90 \pm 0.02$	$-2.39 \pm 0.04$	$-2.40 \pm 0.04$	$-2.42 \pm 0.04$	$-2.48 \pm 0.04$	$-2.56 \pm 0.04$
	outer	$2.84 \pm 0.11$	$0.58 \pm 0.03$	$24.25 \pm 0.02$	$-1.77 \pm 0.04$	$-1.76 \pm 0.07$	$-1.88 \pm 0.08$	$-1.86 \pm 0.11$	$-1.79 \pm 0.17$
NGC 4163	inner	$2.95 \pm 0.08$	$0.47 \pm 0.02$	$21.92 \pm 0.02$	$-1.87 \pm 0.03$	$-1.91 \pm 0.04$	$-2.32 \pm 0.03$	$-2.48 \pm 0.04$	$-2.54 \pm 0.05$
	outer	$2.95 \pm 0.08$	$0.67 \pm 0.02$	$23.50 \pm 0.02$	$-1.78 \pm 0.03$	$-1.78 \pm 0.05$	$-2.30 \pm 0.03$	$-2.42 \pm 0.05$	$-2.42 \pm 0.06$
KDG 90		$3.02 \pm 0.12$	$0.59 \pm 0.03$	$24.00 \pm 0.02$	$-2.21 \pm 0.03$	$-2.20 \pm 0.03$	$-2.19 \pm 0.04$	$-2.19 \pm 0.05$	$-2.17 \pm 0.06$
DDO 44		$3.25 \pm 0.10$	$0.63 \pm 0.03$	$24.28 \pm 0.02$	$-2.02 \pm 0.08$	$-1.98 \pm 0.17$	$-1.94 \pm 0.32$	$-2.03 \pm 0.30$	$-2.00 \pm 0.35$
DDO 6		$3.40 \pm 0.15$	$0.23 \pm 0.03$	$23.65 \pm 0.02$	$-2.16 \pm 0.04$	$-2.42 \pm 0.04$	$-2.60 \pm 0.04$	$-2.86 \pm 0.05$	$-3.15 \pm 0.06$
KDG 61		$3.63 \pm 0.10$	$0.76 \pm 0.03$	$23.50 \pm 0.02$	$-1.50 \pm 0.04$	$-1.49 \pm 0.04$	$-1.49 \pm 0.04$	$-1.49 \pm 0.04$	$-1.48 \pm 0.05$
BK5N		$3.71 \pm 0.10$	$0.81 \pm 0.02$	$23.36 \pm 0.02$	$-1.73 \pm 0.03$	$-1.73 \pm 0.03$	$-1.73 \pm 0.03$	$-1.72 \pm 0.04$	$-1.71 \pm 0.04$
KDG 64		$3.72 \pm 0.17$	$0.81 \pm 0.03$	$24.71 \pm 0.02$	$-1.71 \pm 0.06$	$-1.72 \pm 0.09$	$-1.70 \pm 0.10$	$-1.69 \pm 0.12$	$-1.69 \pm 0.12$
KG 1207	inner	$4.88 \pm 0.32$	$0.33 \pm 0.03$	$21.57 \pm 0.02$	$-2.15 \pm 0.05$	$-2.16 \pm 0.05$	$-2.17 \pm 0.05$	$-2.20 \pm 0.04$	$-2.35 \pm 0.03$
	outer	$4.88 \pm 0.32$	$0.57 \pm 0.04$	$24.19 \pm 0.03$	$-1.52 \pm 0.05$	$-1.67 \pm 0.07$	$-1.65 \pm 0.07$	$-1.64 \pm 0.08$	$-1.80 \pm 0.10$
UGC 5423	inner	$8.36 \pm 0.29$	$0.27 \pm 0.06$	$23.53 \pm 0.04$	$-2.46 \pm 0.05$	$-2.46 \pm 0.06$	$-2.59 \pm 0.04$	$-2.79 \pm 0.05$	$-2.79 \pm 0.03$
	outer	$8.71 \pm 0.24$	$0.42 \pm 0.02$	$22.24 \pm 0.02$	$-2.09 \pm 0.05$	$-2.39 \pm 0.04$	$-2.44 \pm 0.03$	$-2.53 \pm 0.03$	$-2.61 \pm 0.03$
AGC 111946		$8.71 \pm 0.24$	$0.62 \pm 0.03$	$23.70 \pm 0.02$	$-1.76 \pm 0.07$	$-1.77 \pm 0.07$	$-1.80 \pm 0.08$	$-1.80 \pm 0.10$	$-1.80 \pm 0.11$

NOTE— $^\dagger$  Calculated in the area used for SBF calculation, with  $M_{g,\text{thres}} = -4.0$  mag. Errors include HSC calibration error 0.017 mag (Aihara et al. 2019) per each band.

large an area including the low surface brightness region,  $P_0$  fluctuations from contaminating sources as well as from true SBF signals are amplified. The background subtraction procedure can mitigate this effect since the fluctuation power from background sources (e.g. background galaxies) increases as well. However, errors in background subtraction unnecessarily increase in this case. Also, using too small an area is not recommended because it results in poor fits to the power spectrum due to the small number of pixels. So, we measured the SBF using various annular masks and selected an area based on the galaxy’s surface brightness and size. Solid line ellipses in Figure 1 are annular mask boundaries of inner fields and dotted line rings are those of outer fields. The color and mean surface brightness of the selected areas for SBF measurements of the sample galaxies are listed in Table 2.

### 3.3.2. Individual Source Mask

There are two kinds of contaminating sources that should not be included in calculating the SBF: (1) background objects such as faint galaxies and foreground Milky Way stars, and (2) young stellar populations of the galaxy. Contribution from background objects can be successfully taken into account in two steps as described in Carlsen et al. (2019b). First, objects brighter

than a masking threshold are masked when calculating galaxy fluctuation power  $P_0$ . Second, contributions from objects fainter than the threshold are statistically estimated and subtracted by measuring the background fluctuations in flat fields well away from the galaxy, within a radius of 0.2 degrees (PSF-scale components in Figure 2(f) and (l)), which are masked using the same threshold. When using a brighter masking threshold, one would obtain a larger galaxy fluctuation and a larger background fluctuation, so the difference should remain approximately constant. Therefore, the choice of masking threshold does not yield any significant systematic uncertainties in the SBF measurement of red galaxies unless one uses a faint magnitude threshold that masks the galaxy’s asymptotic giant branch (AGB) and red giant branch (RGB) stars, which produce the desired SBF signal.

In contrast, young stellar populations are trickier to handle and the choice of masking thresholds may lead to systematic uncertainties. Young massive blue stars are small in number, but they are very bright and are clumped in star forming regions, contributing to large fluctuations. Therefore, they result in significant SBF and stochastic effects and it is important to avoid including star forming regions in SBF calculation.

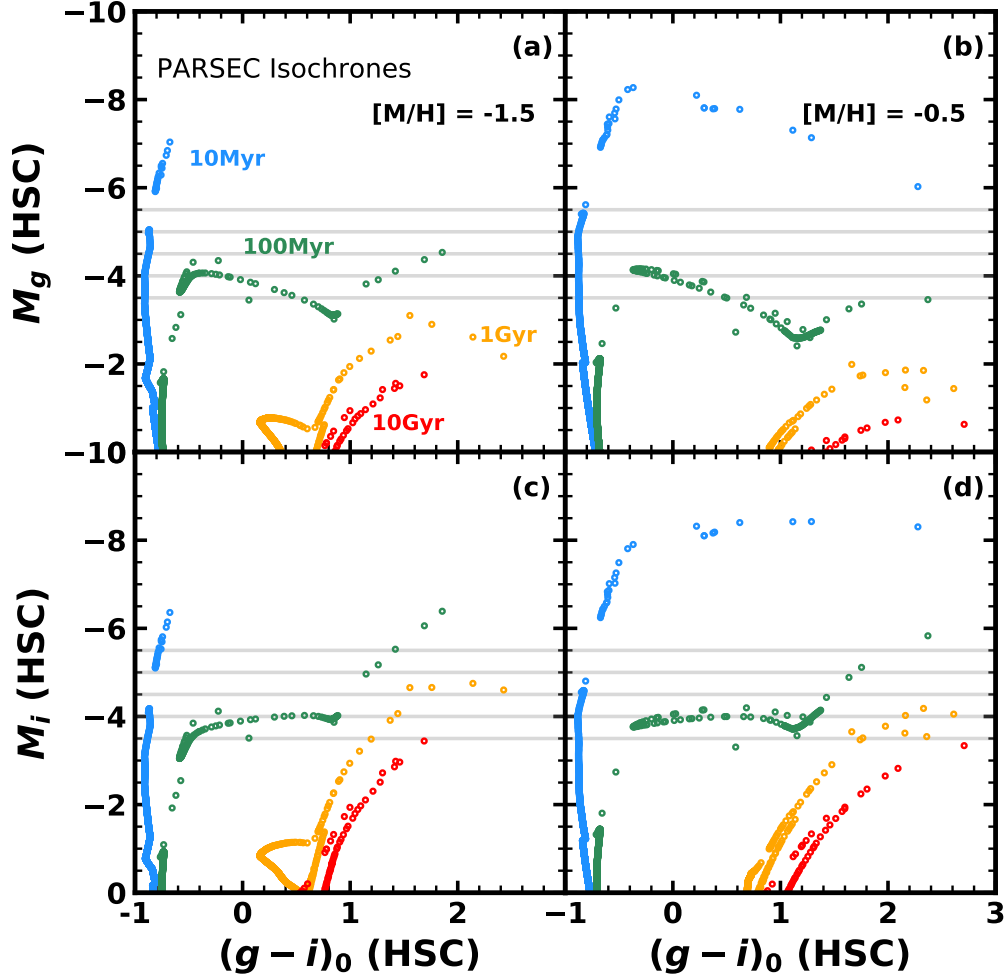


**Figure 3.** Color-magnitude diagrams of simulated populations with a total mass of  $10^5 M_\odot$  from PARSEC evolutionary tracks. Upper panels (a and b) represent  $M_g$  versus  $(g-i)_0$  and lower panels (c and d) represent  $M_i$  versus  $(g-i)_0$ . Left panels (a and c) and right panels (b and d) display metal-poor ( $[M/H] = -1.5$ ) and metal-rich ( $[M/H] = -0.5$ ) populations, respectively. Colors indicate stellar isochrones for four ages (10 Myr, 100 Myr, 1 Gyr, and 10 Gyr). Gray horizontal lines indicate the five masking thresholds ( $M_{g,\text{thres}}$ ) used in this study.

To show the effect of young stellar populations, we plot, in Figure 3, color-magnitude diagrams of simulated simple stellar populations with a total mass of  $10^5 M_\odot$  from PARSEC evolutionary tracks (Bressan et al. 2012)<sup>3</sup>, for ages 10 Myr, 100 Myr, 1 Gyr, and 10 Gyr. PARSEC tracks are a revised version of the former Padova tracks, computed for a scaled-solar composition and following the helium abundance  $Y = 0.2485 + 1.78Z$ . PARSEC computes stellar evolution from the pre main-sequence to the onset of the first thermal pulsation. The evolution of TP-AGB stars is traced with COLIBRI codes (Marigo et al. 2013, 2017), from the first thermal pulsation to the total loss of the envelope. Circles in the left panels

(a and c) and in the right panels (b and d) represent metal-poor ( $[M/H] = -1.5$ ) and metal-rich populations ( $[M/H] = -0.5$ ), respectively. Stellar populations that are bright in  $i$ -band are the main contributors to the  $i$ -band SBF. If a galaxy lacks young stellar populations and consists of intermediate-age and old stellar populations, RGB and AGB stars dominate its SBF. However, if young stellar populations are present, massive main sequence stars, core helium burning stars, and supergiant stars would contribute to larger fluctuations. A majority of the young stellar populations have bluer colors than older stellar populations so they are more prominent in  $g$ -band magnitudes than in  $i$ -band magnitudes.

We check for systematic effects with five masking thresholds:  $M_g = -3.5, -4.0, -4.5, -5.0$ , and  $-5.5$  mag, indicated as gray horizontal lines in Figure 3. We use

<sup>3</sup> <http://stev.oapd.inaf.it/cmd>



**SExtractor** (Bertin & Arnouts 1996) to detect contaminating objects. All the objects brighter than a threshold are masked using segmentation maps generated by the **SExtractor**, which indicate the pixels belonging to each detected source. Masking objects in the range  $-5.5 \leq M_g \leq -3.5$  would mask unresolved young star clusters, bright blue main-sequence stars, core helium burning stars, and supergiant stars, while leaving intermediate-age AGB stars and old RGB stars unmasked. However, absolute  $i$ -band magnitudes of intermediate-age AGB stars lie in the range  $M_i \lesssim -4$ , and SBFs are expected to vary significantly according to the choice of masking thresholds in  $i$ -band magnitudes. Therefore, using  $g$ -band images to detect contaminating sources is favored over using  $i$ -band images. Red objects that are fainter than the  $g$ -band threshold but do not look like fluctuation within the galaxy are additionally masked by visual inspection.

With the chosen masking threshold, objects in nearby background fields are masked as well. The background fluctuation power ( $P_{0,back}$ ) is the PSF-scaled power ( $P_0$  in Equation 1) of  $(\text{Background})/\sqrt{\text{Model}}$ . We calculate  $P_{0,back}$  in 100 random nearby background areas, and adopt its median value. Then we obtain background-subtracted SBF power by subtracting the median  $P_{0,back}$  from  $P_0$ . We use  $1\sigma$  range of  $P_{0,back}$  as a background subtraction error.

Small contours in Figure 2(a) and (g) represent masked sources. The dark blue, light blue, cyan, light green, and orange contours indicate sources masked using thresholds of  $M_g = -3.5, -4.0, -4.5, -5.0$ , and  $-5.5$  mag. While BK5N shows only a few bright blue sources, in the central elliptical area used for calculating the SBF, DDO 6, has many such sources with various magnitudes. The effects of using different masking thresholds are discussed in Section 4.1.

### 3.4. Power Spectrum Fitting

We fit the power spectra (right panels of Figure 2) to the linear function (Equation 1) by the least-squares method. Dashed red lines represent the PSF-scale fluctuation component  $P_0 E(k)$  and dotted lines represent the white noise component ( $P_1$ ). The lowest wavenumbers and the highest wavenumbers (gray shaded regions in right panels in Fig 2) are excluded from the fitting range. This is because the lowest wavenumbers are affected by large scale subtraction errors due to imperfect galaxy models and the highest wavenumbers are affected by pixel interpolations introduced when stacking images. The minimum wavenumber is chosen typically in the range  $[0.03, 0.08] \text{ pix}^{-1}$  and the maximum wavenumber is chosen in the range  $[0.3, 0.4] \text{ pix}^{-1}$ . We iterate

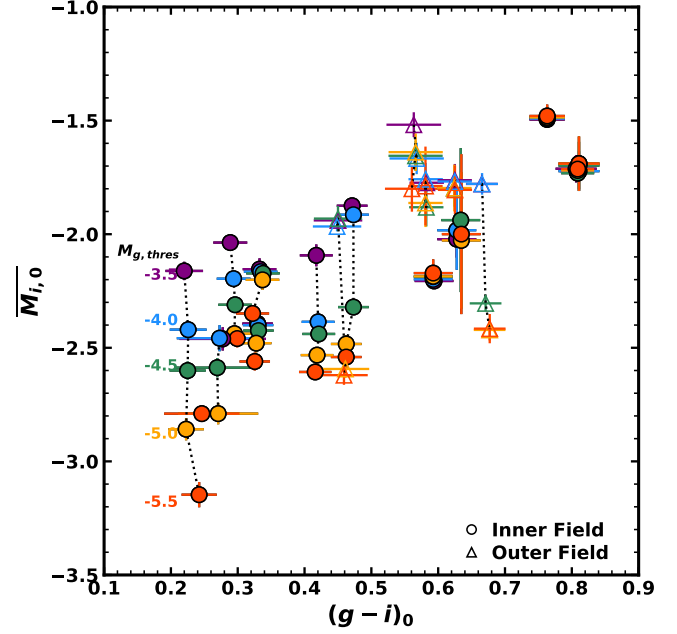


**Figure 4.** SBF absolute magnitude versus integrated color for the calibration sample galaxies. Symbol colors indicate masking thresholds, of which red, orange, green, blue, purple colors represent  $M_{g,thres} = -5.5, -5.0, -4.5, -4.0$ , and  $-3.5$  mag respectively. Circles and triangles indicate inner and outer regions of the galaxies, respectively.

the fitting procedure to find the best ranges. The uncertainty introduced by variable fitting range is determined as one-sigma range of results from multiple fits. Measurement errors of SBF correspond to the quadratic sum of background subtraction error and power spectrum fitting error.

## 4. SBF CALIBRATION

We derive the SBF apparent magnitudes of 17 fields in 12 dwarf galaxies using the method described in the previous section. Using the TRGB distances to the galaxies, we obtain the SBF absolute magnitudes,  $\overline{M}_i$ . The results are listed in Table 2. The listed errors in  $\overline{M}_i$  include SBF measurement errors. In this section, we derive SBF and integrated color relations for the HSC  $i$ -band. But first, we check how the choice of masking thresholds  $M_{g,thres}$  affects SBF magnitudes.

### 4.1. Dependence on Masking Thresholds

Figure 4 shows SBF and integrated color relations for our 17 fields. Circular symbols and triangle symbols indicate inner and outer regions of the galaxies, respectively. Symbol colors represent  $M_{g,thres}$ , of which red, orange, green, blue, and purple colors show  $-5.5, -5.0, -4.5, -4.0$ , and  $-3.5$  mag. In general, using fainter  $M_{g,thres}$

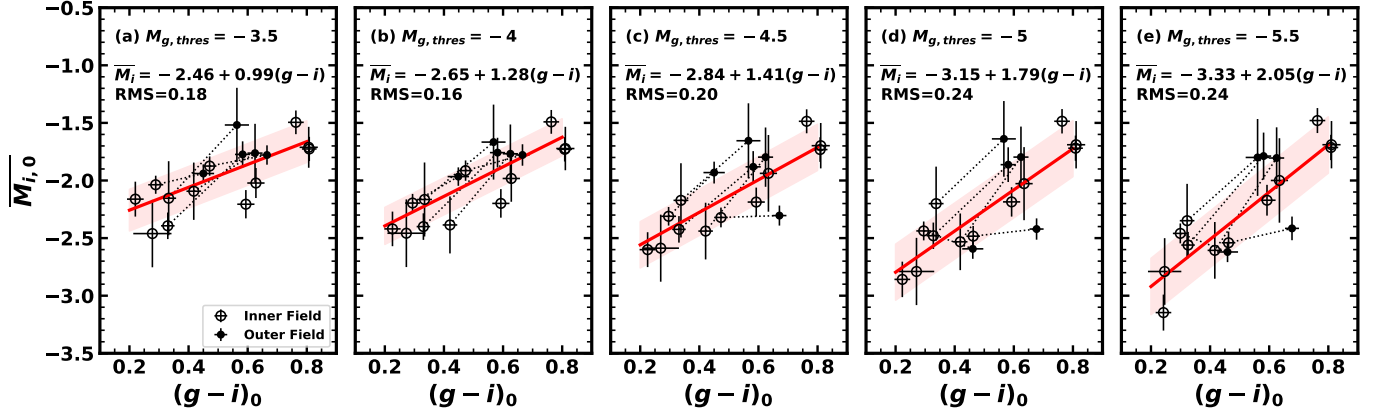


**Figure 5.** SBF and integrated color relations of the calibration sample, with  $M_{g,\text{thres}} = -3.5, -4.0, -4.5, -5.0$ , and  $-5.5$  mag. Open circles and filled circles indicate inner and outer regions of the galaxies, respectively. Linear fits are shown as red lines.

**Table 3.** Fluctuation - Integrated Color Relation Fitting Results

$y_i = \alpha + \beta \times x_i + \epsilon_i, \epsilon_i \sim N(0, \sigma_{int}^2)$				
$M_{g,\text{thres}}$	$\alpha$	$\beta$	$\sigma_{int}$	rms
-3.5	$-2.46 \pm 0.14$	$1.01 \pm 0.24$	$0.11 \pm 0.05$	0.18
-4.0	$-2.65 \pm 0.13$	$1.28 \pm 0.24$	$0.09 \pm 0.05$	0.16
-4.5	$-2.84 \pm 0.18$	$1.41 \pm 0.32$	$0.18 \pm 0.06$	0.20
-5.0	$-3.15 \pm 0.20$	$1.79 \pm 0.36$	$0.21 \pm 0.06$	0.24
-5.5	$-3.33 \pm 0.20$	$2.08 \pm 0.38$	$0.21 \pm 0.07$	0.24

results in fainter fluctuations. While SBF magnitudes of most of the fields in the color range  $(g-i)_0 \gtrsim 0.6$  do not vary significantly according to  $M_{g,\text{thres}}$ , bluer fields show a larger variation. This is because bluer galaxies have more sources in the magnitude range between  $-5.5 < M_g < -3.5$ , mostly young stellar populations.

#### 4.2. Fitting SBF Magnitude-Color Relations

In Figure 5 we plot SBF absolute magnitude versus integrated color of the dwarf galaxies for five different masking thresholds. The open circles and filled circles indicate measurements of inner and outer regions, respectively. Dotted lines link the measurements of the same galaxy. In general, the fluctuation magnitudes in the inner region are brighter than in the outer region. This radial gradient SBF gradient is likely to be resulting from an age effect, as suggested by Jensen et al. (2015). Young stellar populations in the central region enhance the SBF signals.

We model the fluctuation magnitude and color relation by a linear function with a gaussian intrinsic scatter ( $\sigma_{int}$ ):  $y_i = \alpha + \beta \times x_i + \epsilon_i$ .  $\epsilon_i$  is assumed to follow a normal distribution with a mean 0 and a standard deviation

$\sigma_{int}$ . Then we use `emcee` (Foreman-Mackey et al. 2013), a python implementation of Monte-Carlo Markov Chain ensemble sampler for sampling posterior distributions. We consider errors in both axes,  $x = (g-i)_0$  and  $y = \overline{M}_i$ .  $(g-i)_0$  errors are the quadratic sum of Poisson errors within the area used for SBF measurement, sky fluctuations, and the photometric calibration error 0.017 mag (Aihara et al. 2019) per filter.  $\overline{M}_i$  errors used for the fitting are the quadratic sum of SBF measurement errors and the TRGB distance errors. Table 3 lists fitting results. Red lines in Figure 5 indicate linear fits and shaded red regions show corresponding rms scatter.

In Figure 5, the slope of the relation decreases and the y-intercept increases as fainter masking thresholds are used. The rms scatter is the smallest (0.16 mag) when using  $M_{g,\text{thres}} = -4.0$  and it increases with brighter or fainter masking thresholds. Therefore, the slope and rms scatter of the relation vary depending on how many young stars are masked. If more such sources are masked, the slope and rms scatter decrease. For the case using  $M_{g,\text{thres}} = -4.0$ , the intrinsic scatter is found to be  $\sigma_{int} = 0.09 \pm 0.05$ . The value of  $\sigma_{int}$  depends on the values of input errors of  $(g-i)_0$  and  $\overline{M}_i$ . The  $(g-i)_0$  errors used in this study are likely lower bounds, since we do not quantify errors in global sky subtraction by `hscpipe`. Thus, the value of  $\sigma_{int}$  is likely overestimated.

Considering the minimum rms scatter, we choose output parameters for  $M_{g,\text{thres}} = -4.0$  as our final calibration:

$$\overline{M}_i = (-2.65 \pm 0.13) + (1.28 \pm 0.24) \times (g-i)_0. \quad (2)$$

## 5. COMPARISON WITH PREVIOUS CALIBRATIONS AND STELLAR POPULATION MODELS

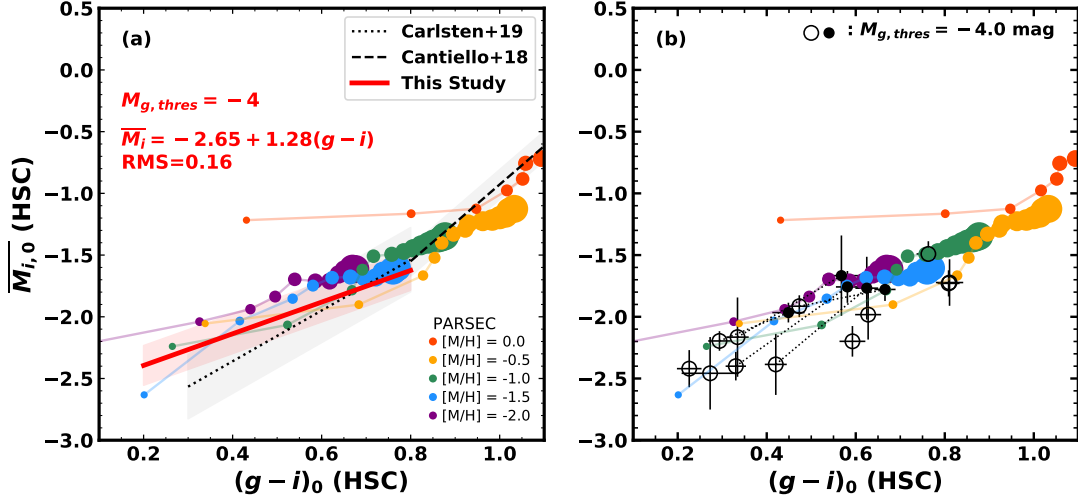


**Figure 6.** (a) Comparison of our SBF calibration for  $M_{g,\text{thres}} = -4.0$  mag (red line) with recent calibrations in the literature (as black lines Carlsten et al. 2019b; Cantiello et al. 2018) and PARSEC models for simple stellar populations. The orange, yellow, green, blue, and purple circles indicate five different metallicities,  $[M/H] = 0.0, -0.5, -1.0, -1.5,$  and  $-2.0$ . Circle sizes indicate relatively ages in the range  $[1, 14]$  Gyr, in a linear spacing, with larger circles being older. (b) Same as the left but with our measured SBFs of the calibration sample as open black (inner fields) and filled black (outer fields) symbols with errorbars.

Figure 6 compares our SBF calibrations with two recent ground-based empirical SBF calibrations (Cantiello et al. 2018; Carlsten et al. 2019b) and PARSEC stellar population models. The SBF absolute magnitudes of stellar population models are computed as luminosity-weighted mean luminosities by integrating weighted stellar isochrones. Our calibration for  $M_{g,\text{thres}} = -4.0$  mag is shown as a red line in Figure 6(a). Our data are plotted with black circles in Figure 6(b). Cantiello et al. (2018), as part of The Next Generation Virgo Cluster Survey (NGVS), used bright red galaxies with  $0.8 < g - i < 1.1$  in the Virgo cluster observed with the CFHT to derive an  $i$ -band calibration (black dashed line). Carlsten et al. (2019b) derived an  $i$ -band calibration in a blue regime ( $0.3 < g - i < 0.8$ ) using 32 LV dwarf galaxies (28 of which are based on CFHT archival data and 6 of which are based on HST data in Cohen et al. (2018)). They showed that the slope of the SBF calibration is shallower in a bluer, metal-poor regime (black dotted line). Since these two calibrations are obtained in the CFHT magnitude system, we transformed them to HSC magnitudes by comparing CFHT and HSC  $g, i$  magnitudes from PARSEC isochrones. While the  $i$ -band magnitudes of the two systems are almost identical in the color range  $0.0 < (g - i) < 1.5$ , their  $g$ -band magnitudes differ slightly, depending on color:  $g_{\text{HSC}} = g_{\text{CFHT}} + 0.045(g - i)_{\text{CFHT}} + 0.006$  (rms=0.002 mag). Using these relations, we obtain  $\overline{M}_{i,\text{HSC}} = -3.18 + 2.06 \times (g - i)_{0,\text{HSC}}$  with rms = 0.26 mag for Carl-

sten et al. (2019b) and  $\overline{M}_{i,\text{HSC}} = -4.04 + 3.11(g - i)_{0,\text{HSC}}$  with rms = 0.12 mag for Cantiello et al. (2018).

Compared to the slope of  $\beta = 2.06 \pm 0.39$  derived by Carlsten et al. (2019b) for the color range similar to that in this study, our derived slope  $\beta = 1.28 \pm 0.24$  is slightly shallower. Also, the rms scatter of our calibration (0.16 mag) is much smaller than that of Carlsten et al. (2019b), 0.26 mag. Among our five calibrations with different masking thresholds, the slopes obtained using  $M_{g,\text{thres}} = -5.0$  and  $-5.5$  mag ( $\beta = 1.79 \pm 0.36$  and  $2.08 \pm 0.38$ ) are similar to that of Carlsten et al. (2019b). In addition, the rms scatter of the two cases, 0.24 mag, is similar to that of Carlsten et al. (2019b), 0.26 mag. Therefore, we conjecture that the average masking done by Carlsten et al. (2019b) is similar to our case of  $M_{g,\text{thres}} = -5.0$  or  $-5.5$  mag.

As suggested by previous studies (Mieske et al. 2006; Blakeslee et al. 2009; Jensen et al. 2015; Carlsten et al. 2019b), the color dependence of SBF absolute magnitude on colors is smaller in the blue regime. Comparing our  $\beta$  with the slope of Cantiello et al. (2018) ( $\beta = 3.11 \pm 0.42$ ) which presented an  $i$ -band SBF calibration with  $g - i$  colors for the red regime, our slope is significantly shallower. At the color between the blue and red regime,  $(g - i)_0 = 0.8$ , our calibration is only  $\sim 0.07$  mag brighter than that of Cantiello et al. (2018), so both calibrations are consistent within the error range.

In Figure 6, the colored circles display theoretical models calculated from PARSEC simple stellar population models, with ages [1, 14] Gyr and metallicities ([M/H])  $[-2.0, 0.0]$ . Symbol colors vary depending on metallicity, and symbol sizes vary depending on relative age. The red regime ( $(g-i)_0 \gtrsim 0.8$  mag) corresponds to metal-rich populations and the models for old ages and high metallicities show a fair agreement with Cantiello et al. (2018). In the blue regime ( $(g-i)_0 \lesssim 0.8$  mag), where both old metal-poor populations and intermediate-age metal-rich populations may be present, the scatter of  $\overline{M}_i$  between models is larger. Generally, the empirical  $\overline{M}_i$  for the blue regime is consistent with simple stellar models for low metallicity. The dwarf galaxies at  $0.6 \lesssim (g-i)_0 \lesssim 0.8$  are consistent with models for old ages, and those at  $0.2 \lesssim (g-i)_0 \lesssim 0.6$  overlap with models for younger ages (a few Gyrs). Despite the potential complicated effects that might result from unmasked young stellar populations in late-type galaxies (see Greco et al. (2021) for a detailed study on effects of young stellar populations), our empirical calibration shows a reasonable agreement with predictions from simple stellar population models.

## 6. SUMMARY

We have derived a new empirical  $i$ -band SBF calibration valid in a blue regime ( $0.2 \lesssim (g-i)_0 \lesssim 0.8$ ) in the HSC magnitude system, using 12 dwarf galaxies ( $D_{\text{TRGB}} < 10$  Mpc) in the SMOKA Science Archive. The sample is composed of various morphological types of dwarf galaxies, from star-forming irregular galaxies to dwarf spheroidal galaxies.

Measuring SBFs of dwarf galaxies with young stellar populations is tricky and requires modifications to standard methods. We described the procedures of SBF analysis, applicable for blue, star-forming galaxies. In

making smooth galaxy models, we used median-filtered images with the filter size of ten times the seeing size instead of fitting a Sérsic profile. In addition, we masked young stellar populations brighter than a  $g$ -band masking threshold,  $M_{g,\text{thres}}$ .

We tried multiple masking thresholds,  $M_{g,\text{thres}} = -3.5, -4.0, -4.5, -5.0$ , and  $-5.5$  mag and derived SBF calibrations for each case, as summarized in Table 3. Using a fainter  $M_{g,\text{thres}}$ , the fluctuations of galaxies in the blue regime systematically decrease and the slope of the SBF calibration gets shallower. In the case of  $M_{g,\text{thres}} = -4.0$  mag, the rms scatter of the linear fit is the smallest, 0.16 mag (Equation 2). This scatter is much smaller than those in the previous studies for dwarf galaxies in the blue regime. Our result shows a reasonable agreement with PARSEC models for metal-poor, intermediate and old simple stellar populations.

Recently Kim et al. (2021) estimated the SBF distances to the dwarf galaxy candidates around NGC 4437 from the HSC data, applying the calibration in this study, and they could identify successfully the members of the NGC 4437 group. The calibration in this study will be very useful for estimating distances to dwarf galaxies in the LV found in the various deep and wide surveys.

## ACKNOWLEDGMENTS

We thank the anonymous referee for providing helpful comments. This work was supported by the National Research Foundation grant funded by the Korean Government (NRF-2019R1A2C2084019). We thank Brian S. Cho for his help in improving the English in this manuscript.

## REFERENCES

- Aihara, H., AlSayyad, Y., Ando, M., et al. 2019, PASJ, 71, 114
- Anand, G. S., Rizzi, L., Tully, R. B., et al. 2021, AJ, 162, 80. doi:10.3847/1538-3881/ac0440
- Bertin, E. & Arnouts, S. 1996, A&AS, 117, 393. doi:10.1051/aas:1996164
- Blakeslee, J. P., Vazdekis, A., & Ajhar, E. A. 2001, MNRAS, 320, 193. doi:10.1046/j.1365-8711.2001.03937.x
- Blakeslee, J. P., Jordán, A., Mei, S., et al. 2009, ApJ, 694, 556. doi:10.1088/0004-637X/694/1/556
- Blakeslee, J. P., Cantiello, M., Mei, S., et al. 2010, ApJ, 724, 657. doi:10.1088/0004-637X/724/1/657
- Blakeslee, J. P., Jensen, J. B., Ma, C.-P., et al. 2021, ApJ, 911, 65. doi:10.3847/1538-4357/abe86a
- Bosch, J., Armstrong, R., Bickerton, S., et al. 2018, PASJ, 70, S5. doi:10.1093/pasj/psx080
- Bressan, A., Marigo, P., Girardi, L., et al. 2012, MNRAS, 427, 127. doi:10.1111/j.1365-2966.2012.21948.x
- Bullock, J. S. & Boylan-Kolchin, M. 2017, ARA&A, 55, 343. doi:10.1146/annurev-astro-091916-055313
- Cantiello, M., Blakeslee, J. P., Raimondo, G., et al. 2005, ApJ, 634, 239. doi:10.1086/491694
- Cantiello, M., Blakeslee, J. P., Ferrarese, L., et al. 2018, ApJ, 856, 126
- Carlin, J. L., Sand, D. J., Price, P., et al. 2016, ApJL, 828, L5. doi:10.3847/2041-8205/828/1/L5
- Carlin, J. L., Mutlu-Pakdil, B., Crnojević, D., et al. 2021, ApJ, 909, 211. doi:10.3847/1538-4357/abe040



- Carlsten, S. G., Beaton, R. L., Greco, J. P., et al. 2019, *ApJL*, 878, L16. doi:10.3847/2041-8213/ab24d2
- Carlsten, S. G., Beaton, R. L., Greco, J. P., et al. 2019, *ApJ*, 879, 13
- Carlsten, S. G., Greco, J. P., Beaton, R. L., et al. 2020, *ApJ*, 891, 144. doi:10.3847/1538-4357/ab7758
- Carlsten, S. G., Greene, J. E., Peter, A. H. G., et al. 2021, *ApJ*, 908, 109. doi:10.3847/1538-4357/abd039
- Cohen, Y., van Dokkum, P., Danieli, S., et al. 2018, *ApJ*, 868, 96. doi:10.3847/1538-4357/aae7c8
- Davis, A. B., Nierenberg, A. M., Peter, A. H. G., et al. 2021, *MNRAS*, 500, 3854. doi:10.1093/mnras/staa3246
- Foreman-Mackey, D., Hogg, D. W., Lang, D., et al. 2013, *PASP*, 125, 306
- Greco, J. P., van Dokkum, P., Danieli, S., et al. 2021, *ApJ*, 908, 24. doi:10.3847/1538-4357/abd030
- Ivezić, Ž., Kahn, S. M., Tyson, J. A., et al. 2019, *ApJ*, 873, 111
- Jacobs, B. A., Rizzi, L., Tully, R. B., et al. 2009, *AJ*, 138, 332. doi:10.1088/0004-6256/138/2/332
- Jang, I. S., Hoyt, T. J., Beaton, R. L., et al. 2021, *ApJ*, 906, 125. doi:10.3847/1538-4357/abc8e9
- Jensen, J. B., Tonry, J. L., & Luppino, G. A. 1998, *ApJ*, 505, 111. doi:10.1086/306163
- Jensen, J. B., Tonry, J. L., Barris, B. J., et al. 2003, *ApJ*, 583, 712. doi:10.1086/345430
- Jensen, J. B., Blakeslee, J. P., Gibson, Z., et al. 2015, *ApJ*, 808, 91. doi:10.1088/0004-637X/808/1/91
- Jerjen, H., Freeman, K. C., & Binggeli, B. 1998, *AJ*, 116, 2873
- Jerjen, H., Freeman, K. C., & Binggeli, B. 2000, *AJ*, 119, 166. doi:10.1086/301188
- Jerjen, H., Rekola, R., Takalo, L., et al. 2001, *A&A*, 380, 90. doi:10.1051/0004-6361:20011408
- Karachentsev, I. D., Makarov, D. I., & Kaisina, E. I. 2013, *AJ*, 145, 101. doi:10.1088/0004-6256/145/4/101
- Kim, Y. J., Kang, J., Lee, M. G., & Jang, I. S. 2021, *ApJ*, submitted
- Klypin, A., Kravtsov, A. V., Valenzuela, O., et al. 1999, *ApJ*, 522, 82. doi:10.1086/307643
- Lee, M. G., Freedman, W. L., & Madore, B. F. 1993, *ApJ*, 417, 553
- Liu, M. C., Charlot, S., & Graham, J. R. 2000, *ApJ*, 543, 644. doi:10.1086/317147
- Marigo, P., Bressan, A., Nanni, A., et al. 2013, *MNRAS*, 434, 488. doi:10.1093/mnras/stt1034
- Marigo, P., Girardi, L., Bressan, A., et al. 2017, *ApJ*, 835, 77. doi:10.3847/1538-4357/835/1/77
- Mei, S., Blakeslee, J. P., Tonry, J. L., et al. 2005, *ApJS*, 156, 113
- Mieske, S., Hilker, M., & Infante, L. 2006, *A&A*, 458, 1013. doi:10.1051/0004-6361:20054685
- Moore, B., Ghigna, S., Governato, F., et al. 1999, *ApJL*, 524, L19. doi:10.1086/312287
- Müller, O. & Jerjen, H. 2020, *A&A*, 644, A91. doi:10.1051/0004-6361/202038862
- Peng, C. Y., Ho, L. C., Impey, C. D., et al. 2002, *AJ*, 124, 266. doi:10.1086/340952
- Schlafly, E. F., & Finkbeiner, D. P. 2011, *ApJ*, 737, 103
- Schlegel, D. J., Finkbeiner, D. P., & Davis, M. 1998, *ApJ*, 500, 525
- Smercina, A., Bell, E. F., Price, P. A., et al. 2018, *ApJ*, 863, 152. doi:10.3847/1538-4357/aad2d6
- Tonry, J., & Schneider, D. P. 1988, *AJ*, 96, 807
- Tonry, J. L., Ajhar, E. A., & Luppino, G. A. 1990, *AJ*, 100, 1416. doi:10.1086/115606
- Tully, R. B., Rizzi, L., Shaya, E. J., et al. 2009, *AJ*, 138, 323. doi:10.1088/0004-6256/138/2/323
- van Dokkum, P., Danieli, S., Cohen, Y., et al. 2018, *Nature*, 555, 629. doi:10.1038/nature25767